A study on the Microstructure and Mechanical Properties of the Ti-6Al-2Sn-4Zr-6Mo Alloy Produced via Laser Powder Bed Fusion

Journal of Alloys and Compounds 870 (2021) 159329

Contents lists available at ScienceDirect

Journal of Alloys and Compounds

journal homepage: www.elsevier.com/locate/jalcom

A study on the microstructure and mechanical properties of the Ti-6Al-2Sn-4Zr-6Mo alloy produced via Laser Powder Bed Fusion

Alessandro Carrozza*, Alberta Aversa, Paolo Fino, Mariangela Lombardi

Department of Applied Science and Technology, Politecnico Di Torino, Corso Duca degli Abruzzi 24, Torino 10129, Italy

ARTICLE INFO

Article history:
Received 5 December 2020
Received in revised form 1 February 2021
Accepted 23 February 2021
Available online 25 February 2021

Keywords:
Additive manufacturing
Laser Powder Bed Fusion
Titanium alloys
Mechanical properties
Heat treatment

ABSTRACT

Laser Powder Bed Fusion (LPBF) is an additive manufacturing technology which has been the subject of thorough research and successfully adopted in several industrial sectors. Among all the processable classes of materials, titanium alloys are especially interesting due to their favourable combination of mechanical properties and corrosion resistance. Most of the literature focuses on Ti-6Al-4V, although there are other alloys which are widely applied in fields that can benefit from the advantages of LPBF techniques, such as Ti-6Al-2Sn-4Zr-6Mo, thus far not investigated for this technology. This alloy is generally preferred to Ti-6Al-4V for the production of some components in the aerospace industry, mostly due to its superior strength. In this work, the most suitable process window for this alloy was investigated. Samples produced with two different combinations of process parameters, located in the selected process window, were then thoroughly studied in order to assess the effect of building conditions on the microstructure, phases and mechanical properties of the as-built and heat-treated material. To do so, an X-ray diffraction analysis was conducted with the aim of determining the phase composition and lattice parameters. Moreover, microstructural features, such as α" needles and α lath widths, were analysed in order to correlate the thermal history of the process to the final microstructure of the specimens. Furthermore, the hardness and the tensile properties of the alloy processed by LPBF were quantified and compared with the data available in the literature relative to conventional manufacturing technologies.

1. Introduction

Titanium alloys are a class of metals which are particularly appreciated in several industrial fields due to their extremely high strength-to-weight ratio, corrosion resistance and biocompatibility [1–3]. At near room temperature, titanium alloys can be composed of either mainly α phase, β phase or both. This depends on the composition of the starting material, as the alloying elements can be either α stabilizers (e.g. Al, O, N) or β stabilizers (e.g. Mo, V, Fe) [1,4]. According to the main phase of the material, titanium alloys can therefore be split into three groups: α alloys, α + β (or duplex) alloys and β alloys. Since the β phase is unstable in pure titanium below 882 °C [1], a possible way to establish the effect of the alloying elements on a generic alloy is the beta stability index (SI_β) [5–7], which roughly determines how prone the material is to retaining metastable β phase at room temperature, and is calculated as:

$$SI_\beta = [Mo]_{EQ} - [Al]_{EQ}\,(wt.\,\%) \tag{1}$$

where $[Mo]_{EQ}$ and $[Al]_{EQ}$ represent the equivalent molybdenum and aluminium concentrations, respectively. These parameters can be calculated as:

$$[Mo]_{EQ} = [Mo] + \frac{2}{3}[V] + \frac{1}{3}[Nb] + 3([Fe] + [Cr]) \tag{2}$$

$$[Al]_{EQ} = [Al] + \frac{1}{3}[Sn] + \frac{1}{6}[Zr] + 10([C] + [O] + 2[N]) \tag{3}$$

Ti-6Al-2Sn-4Zr-6Mo (Ti6246) is a high-strength duplex alloy which is mainly used in compressor disks and blades in aero gas turbine engines and in some high temperature sections of race car engines [5,8]. The importance of this alloy is mainly due to its ability to retain good mechanical properties at relatively high temperatures. Moreover, it is generally adopted as a replacement for the Ti-6Al-4V alloy for specific applications (e.g. compressor parts in aero-engines) in which a higher strength is needed [7,9]. Compared to the duplex alloy Ti-6Al-4V (Ti64), Ti6246 has a higher beta stability index ($SI_{\beta,Ti6246} = -1.33$ and $SI_{\beta,Ti64} = -3.33$), which is the main reason why it is often defined as a near-β alloy, as a greater amount of β phase is

* Corresponding author.
E-mail addresses: alessandro.carrozza@polito.it (A. Carrozza), alberta.aversa@polito.it (A. Aversa), paolo.fino@polito.it (P. Fino), mariangela.lombardi@polito.it (M. Lombardi).

https://doi.org/10.1016/j.jallcom.2021.159329
0925-8388/

retained at near room temperature [10,11]. In addition, Ti6246 is characterized by a lower Young's modulus (E) [7] and an increased ductility [4] than Ti64. Moreover, previous studies [12] highlighted how an increase in β phase stability causes a shift from hexagonal to orthorhombic martensite in rapidly cooled titanium alloys [12], which is the most significant microstructural difference between Ti6246 and Ti64. In fact, the latter forms α' martensite (hexagonal) upon fast cooling from T > martensite start (M_S) (≈800 °C) as a result of the martensitic β → α' transformation, kinetically favoured over the thermodynamically more stable, and diffusion-driven, β → α + β transformation [13,14]. This type of martensite results in a ductility reduction due to its ability to hinder dislocation motion, having a very moderate strengthening effect [1,2,13]. On the contrary, Ti6246 forms α" martensite (orthorhombic) upon fast cooling from T > M_S (≈880 °C), following a path similar to the former alloy [12,15–17] but increasing the ductility of the alloy and softening the material [18]. Both α' and α" crystallize in a lath morphology and their microstructural features are usually referred to as needles, due to their elongated shape [15].

The term "Additive Manufacturing" (AM) is used to describe a family of innovative and disruptive production technologies which allow near-net-shape products to be built directly from a computer-aided design (CAD) file [19,20]. AM technologies appear particularly promising in fields where high-quality, highly customisable and very complex parts are needed (e.g. aerospace, biomedical). Small production lots, which are usually not economically viable for conventional technologies, are also another interesting application of AM technologies. All these features are particularly favourable in industrial sectors in which Ti6246 is already in use, such as the automotive and aerospace fields.

Among metal AM technologies, Laser Powder Bed Fusion (LPBF) systems allow the production of components using several high-performance types of alloys, such as nickel-based [21,22], aluminium [23,24] and steels [25,26]. The LPBF of titanium alloys has been thoroughly investigated in recent years. Although, most of the works available in the literature focus on Ti64 [27–29], some works on other titanium alloys can be found, such as commercial purity titanium (cp-Ti) [30], Ti-6Al-7Nb [31], Ti-24Nb-4Zr-8Sn [32] and Ti-21Nb-17Zr [33]. However, according to the authors' knowledge, no works on LPBF-produced Ti6246 have been published so far. Nevertheless, Gebisa et al. [34] already stated the importance of investigating the possibility of manufacturing Ti6246 components using powder-bed AM technologies, especially for compressor production in the aerospace field.

For these reasons, in this work the LPBF processability of the Ti-6Al-2Sn-4Zr-6Mo alloy has been investigated. First of all, several combinations of process parameters were studied in order to find the most suitable process window, using porosity minimization as a defining criterion. Moreover, the influence of the process parameters on the microstructure, hardness and tensile properties of the samples was also assessed. Finally, the significance and the effect of a post-processing heat treatment was studied.

2. Materials and methods

The samples studied in this investigation were built via LPBF using an EOS M270 Xtended machine and processing a Ti-6Al-2Sn-4Zr-6Mo gas-atomized pre-alloyed powder, provided by TLS Technik GmbH. The nominal chemical composition of the powder, as declared by the supplier, is summarised in Table 1.

The particle size distribution of the Ti6246 powder was defined by analysing several scanning electron microscope (SEM) images, resulting in a D(10), D(50) and D(90) of 24.1, 38.0 and 54.7 µm respectively. The powder was characterized by a bimodal particle size distribution, provided in Fig. 1a, with a primary peak at approximately a 40 µm value and a secondary peak at 5–10 µm. This effect

Table 1
Nominal chemical composition (wt%) of the Ti-6Al-2Sn-4Zr-6Mo powder.

Chemical element	Composition range (wt%)
Al	5.5 – 6.5
Sn	1.75 – 2.25
Zr	3.5 – 4.5
Mo	5.5 – 6.5
Fe	<0.15
O	<0.15
N	<0.04
C	<0.04
H	<0.125
other	<0.4
Ti	bal.

can be attributed to the large amount of small particles in the powder, as visible in Fig. 1b. Acknowledging this information is important, as the particle size distribution directly impacts on the powder ability to pack efficiently and its rheological behaviour [35].

A first series of 36 15 × 15 × 15 mm samples was built in order to evaluate the most suitable parameters to process the Ti6246 powder. Different values of laser power (P), scanning speed (v) and hatching distance (h.d.) were fixed, as described in Table 2, for a total of 18 different parameters combinations. Among them, the combination of process parameters of the standard Ti64 powder with a P of 170 W, a v of 1250 mm/s and an h.d. of 0.1 mm, was used [36]. This choice was made on the assumption that, as Ti64 is a titanium α + β alloy too, the optimized process parameters for these two materials might be similar. The other parameters, such as temperature platform (T_P), layer thickness (t) and the scanning strategy, were kept constant.

Volumetric Energy Density (VED) was then chosen as a suitable variable to describe the influence of multiple process parameters (P, v, t, h.d.) simultaneously. It is calculated as:

$$VED = \frac{P}{v \cdot t \cdot h\,.\,d.} \tag{4}$$

All the specimens were then cut along the building direction, mounted and polished in order to obtain metallographic samples. Porosity was evaluated by image analysis on 20 optical micrographs per samples (100x magnification) taken throughout the whole sample in as unbiased way.

In a second job, 15 × 15 × 15 mm cubic and 100 mm horizontally oriented cylindrical samples (12.5 mm diameter) were built, using two of the most promising parameters combinations, selected on the basis of porosity values. A part of these specimens was then annealed at 750 °C for 2 h, in order to study the microstructural changes caused by the heat treatment. The specimens were left to cool inside the furnace, achieving a slow cooling of approximately 1.5–2 °C/min. The heat treatment was carried out using A VF800/S high-vacuum furnace (Pro.Ba, Cambiano, TO, Italy).

The as-built and heat-treated cubic samples built using the optimised parameters were then cut along the building direction, polished and etched using a Kroll solution (93% H_2O, 5% HNO_3, 2% HF) in order to investigate the microstructure both by optical and SEM imaging. To do so, a Leica DMI 5000 M optical microscope and a Phenom-XL electron microscope were used. Microstructural features, such as the pore aspect ratio, α/α" widths and amount of β phase present, were evaluated using high-magnification SEM or optical micrographs, processed by the software ImageJ. More than 25 images per condition were analysed.

XRD (X-Ray Diffraction) analyses were also performed to achieve a further understanding of the phases involved and to determine the relative crystallographic parameters. To achieve that, a PANalytical X-Pert Philips diffractometer was deployed. The analyses were recorded at 40 kV and 40 mA in a Bragg Brentano configuration, using a Cu K_α radiation. A step size of 0.013° and a 2θ range between

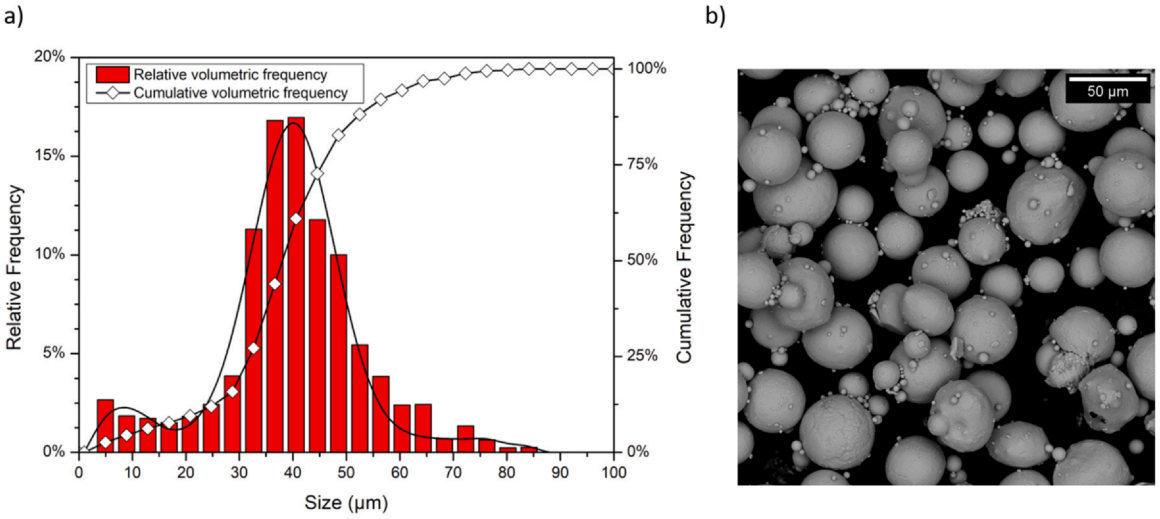

Fig. 1. Particle size distribution of the Ti-6Al-2Sn-4Zr-6Mo powder used in this work (a) with relative representative SEM image (b).

Table 2
Process parameters values considered for the investigation.

P (W)	v (mm/s)	h.d. (mm)	T_P (°C)	t (μm)	Scanning strategy
150, 170, 190	1100, 1250, 1400	0.1, 0.13	100	30	Standard 67° EOS strategy

30° and 60° were considered. In order to grant an acceptable level of comparability between different samples, all the measurements were conducted on samples cut perpendicularly to the baseplate.

In order to evaluate the influence of processing and post-processing conditions, the mechanical behaviour of Ti6246 samples were studied. Hardness measurements of as-built and heat-treated samples were conducted using a Leica VMHT microhardness tester. During the test, a load of 300 g was used for a loading time of 15 s. A total of 25 measurements per samples were taken in different areas of the sample.

Three tensile specimens for each promising process parameter combination and heat treatment condition were obtained by machining as-built/heat-treated cylindric bars, built parallel to the platform. The samples were characterized by a cylindrical shape, as described in ASTM E8 [37], and had a gage length of 16 mm and diameter of 4 mm. The tensile tests were conducted using a Z050 tensile tester (Zwick Roell, Ulm, Germany), operated at strain rate of 0.008 s^{-1}.

3. Results and discussion

3.1. Process parameters determination

The average porosity of the LPBF.produced Ti6246 samples was evaluated by means of image analysis for each combination of considered process parameters. Porosity values were subsequently plotted as a function of VED, as illustrated in Fig. 2. The resulting downward sloping trend provided minimum porosity in correspondence of higher energy densities. In particular, if VED ≥ 40 J/mm^3, for the combinations of process parameters considered in this study, the samples were almost completely dense, providing density values markedly greater than 99%.

As the porosity minimization was chosen as a defining criterion to determine the most suitable process parameter combination, only the samples that provided the highest density values were studied more deeply. The process parameters and relative porosity values for the two chosen sets are listed in Table 3.

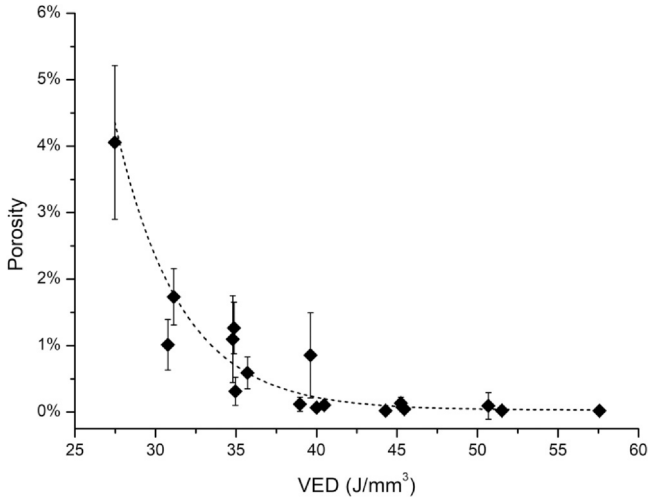

Fig. 2. Mean porosity values as a function of VED for all the sets of parameters considered.

Table 3
Process parameters and porosity values for sets A and B.

Set	Porosity [%]	P [W]	v [mm/s]	h.d. [mm]	VED [J/mm^3]
A	0.01	190	1100	0.1	57.58
B	0.05	150	1250	0.1	40.00

Set A, which is characterised by the highest VED among all the samples analysed, was selected as it presented the minimum porosity value. In contrast, set B was slightly more porous in comparison to the former samples group, but it was characterised by a lower VED and slightly higher build-up rate. Notwithstanding this, the density of all the samples was still greater than 99.9%, which is still a promising outcome for LPBF specimens [38,39]. Set B was chosen as a low-VED sample, making possible to further investigate the effect of energy density on the quality of the LPBF parts through a comparison with the specimens from set A.

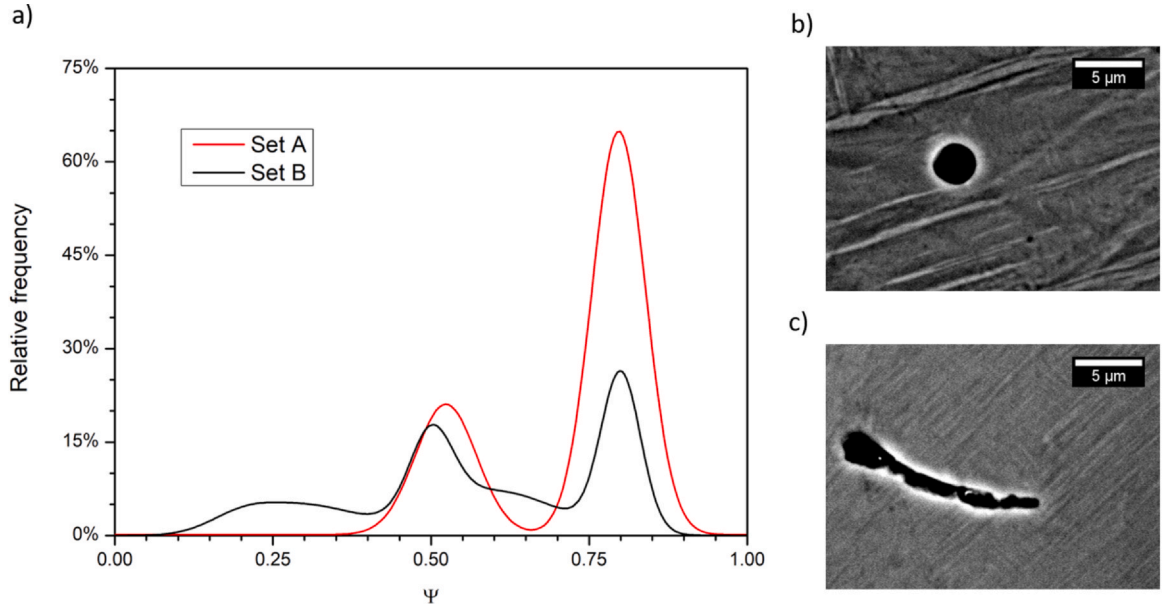

Fig. 3. Relative frequency of pores aspect ratio (Ψ) for sets A and B (a). Representative SEM images of spherical (b) and elongated (c) pores.

Besides the porosity amount, also the mean pore size and pore shape can contribute to a further understanding on the differences between sets A and B. The average pore area (S) was measured via software and then the equivalent diameter (D), which represents the diameter of a hypothetical perfectly circular pore characterized by the same area, was calculated as $D = 2\sqrt{S/\pi}$.

Set A provided a D of 1.20 µm, whilst set B had a D of 2.36 µm. Hence, the samples produced with the lower VED were characterized by larger pores on average. To evaluate the pore shape, according to ISO9276 [40], a specific descriptor of the aspect ratio (Ψ) was selected, which can be calculated as:

$$\Psi = \frac{x_{Fmin}}{x_{Fmax}} \quad (5)$$

Where x_{Fmin} and x_{Fmax} are the minimum and maximum Feret diameters, respectively. In general, $0 < \Psi \leq 1$, where 1 indicates a perfectly circular body. In this case, a higher aspect ratio means that the pore considered is closer to sphericity. An in-depth Ψ investigation was then performed on both sets A and B and the results are plotted in Fig. 3.

Set A was characterised by a larger number of high-Ψ pores, corresponding to quasi-spherical shapes (Fig. 3b), and some intermediate-Ψ pores, providing a bimodal distribution with a minor peak in correspondence of $\Psi \approx 0.5$ and a major peak at $\Psi \approx 0.8$ (Fig. 3a). The latter is predominant, as it accounts for almost 70% of the relative frequency. Instead, set B distribution was broader and more homogeneously distributed throughout the whole Ψ range. In particular, a relevant number of pores in set B specimens were characterised by an aspect ratio lower than 0.35, corresponding to an elongated shape (Fig. 3c). Instead, below this value no pores were detected in set A. In general, elongated pores are usually associated with insufficient energy density values in LPBF-produced titanium alloys [41]. Thus, set A, being characterized by a distribution definitely more shifted towards higher Ψ values, should be more promising in terms of mechanical properties with respect to specimen B.

3.2. Microstructure and phase investigation

The optical micrographs of the samples in the as-built condition are provided in Fig. 4. All the specimens showed prior-β grains, developed in a columnar morphology parallel to the building direction, as highlighted in Fig. 4a. This is a typical microstructure for AM processed titanium alloys due to the very high cooling rates and directional thermal gradients intrinsically involved in the LPBF process [42], which result in β grains epitaxially growing during solidification [28]. Moreover, melt-pool borders are clearly visible in the cross-section (Fig. 4a). The specimens from sets A and B were characterized by elongated needles, arranged in a ± 45° fashion, which are usually associated to the presence of martensite in titanium alloys, when a 0°/90° scanning strategy is adopted [13,15,43]. Martensite formation arises due to a very high cooling rate applied from $T > M_S$. The solidification rates involved in laser processes are extremely high (10^5 to 10^7 °C/s) and consistent with this microstructural feature, since cooling occurs from temperatures that greatly exceed the material M_S [44,45].

At first sight, the optical micrographs of the samples of set A (Fig. 4b) and set B (Fig. 4c) do not show any relevant difference. However, in order to carefully compare the specimens, martensite size was used as an indicator. In particular, martensitic width, already been successfully utilized in previous works for titanium alloys [13,46,47], was measured to properly evaluate the microstructures of in this study. This microstructural feature is strictly correlated to the thermal history of the process and directly influences the mechanical properties of the material [1,13]. The α" width was then evaluated for both sets A and B and studied as a statistical distribution. The results are illustrated in Fig. 5.

The data revealed that set A was characterized by a narrower distribution of α" width, peaking at 0.47 µm and providing an average α" width of 0.54 µm. Instead, set B provided a broader curve, shifted towards higher width values. In fact, its samples had an average α" width of 0.69 µm, and the distribution curve peaked at 0.58 µm. Hence, the specimens from set A were characterised by a finer microstructure.

For a general martensitic transformation, the martensite size is strictly dependant on the thermal history of the material. Previous works available in the literature on α' martensite in Ti64 [13,46] addressed how a larger martensitic feature is associated with a higher cooling rate. A recent experimental study by *Thampy* et al. [48] proved that a higher laser power leads to a lower cooling rate in LPBF-produced Ti64. Working on the same material, Li et al. [49] obtained similar results, as they found that a lower energy density

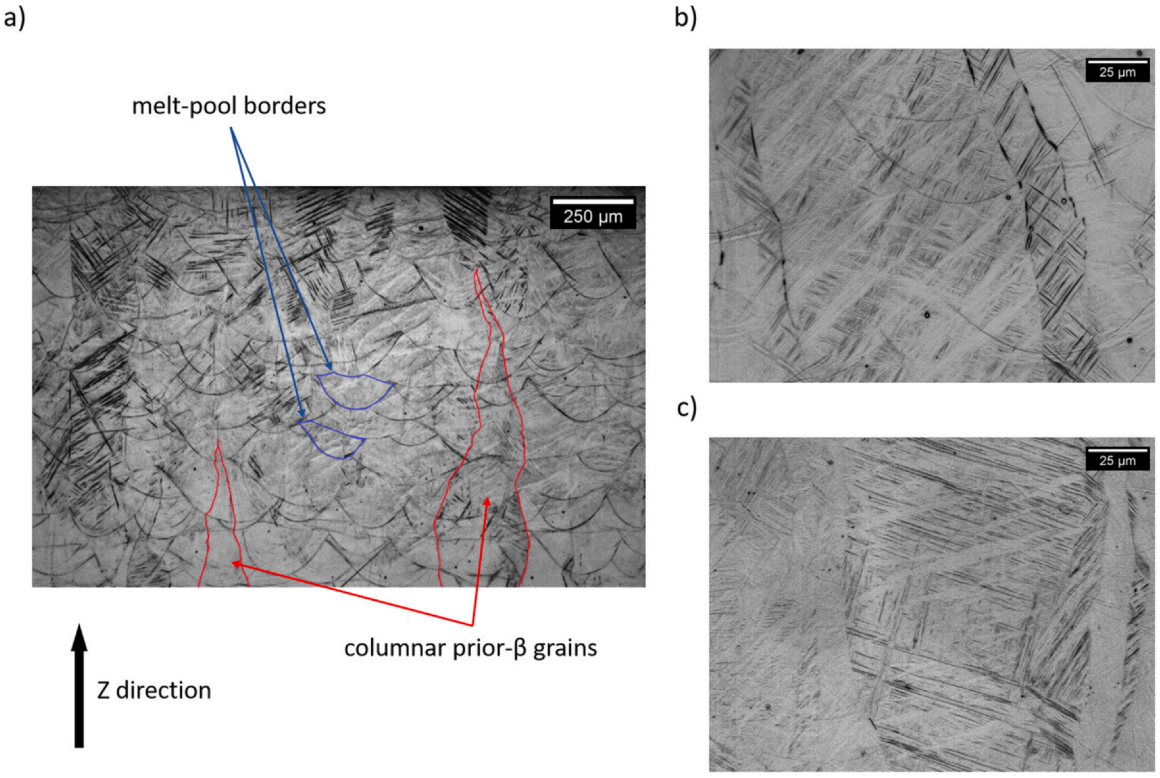

Fig. 4. Representative low-magnification microstructure of the as-built condition, in which some grain boundaries and melt-pool borders are highlighted (a); high-magnification optical micrographs of sets A (b) and B (c).

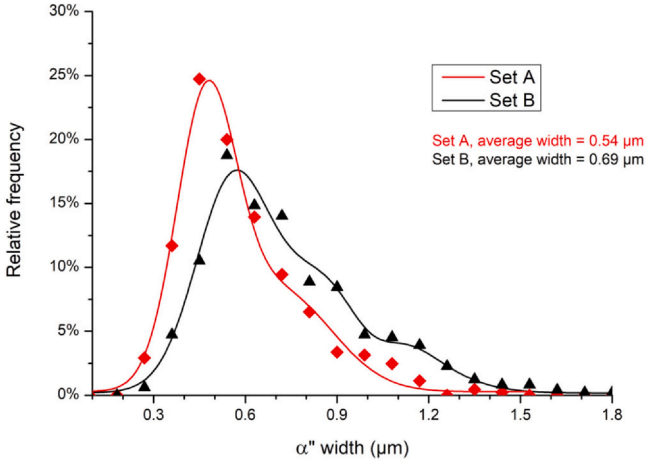

Fig. 5. Relative distribution of α" martensite width for sets A and B.

causes lower solidification times, hence increases the cooling rate. Considering that set A was characterised by higher P and VED values and its martensite appeared finer with respect to set B, the outcome of this evaluation appears in good agreement with the data available in the literature.

Both sets were also heat treated for 2 h at 750 °C, temperature which lies well below the T_β. This sub-β annealing treatment aims to reduce internal stresses and to decompose α", which, as mentioned before, has a negative impact on hardness [18]. The $\alpha'' \rightarrow \alpha + \beta$ transformation is diffusion-driven, requiring high temperature and long times. The resulting micrographs, provided in Fig. 6, demonstrated that, as a consequence of the heat treatment, a complete transformation of the microstructure from martensitic, observed in the as-built state (Fig. 4), to lamellar occurs. Moreover, α phase at prior-β grain boundaries (α_{GB}) was detected. Its formation is typical of duplex titanium alloys and must be carefully controlled because these continuous layers of α phase between prior-β grains can reduce ductility [50]. Even if the microstructures of the heat-treated specimens were mainly lamellar α + β, some traces of larger α aggregates were found, indicating the beginning of the transition of this phase from a lamellar to a globular morphology.

In order to assess if the differences in terms of microstructure in the as-built samples (Fig. 5) were still present after the heat treatment, the lamellar α-phase width was evaluated, in an analogous way with respect to the α" analysis. In these measurements, globular α and α_{GB} were not considered. After the heat treatment, the microstructures of sets A and B appeared markedly more similar and, on the basis of the results of Fig. 7, it can be safely assumed that they are characterised by the same α width. In fact, the average values were very close (0.65 µm for set A and 0.62 µm for set B) and, moreover, the relative distribution curves appeared similar in shape. The sub-β annealing heat treatment assured the elimination of the initial differences, in terms of microstructural size, between sets A and B.

Since β phase was present in a relevant amount in the heat-treated samples, unlike in the as-built ones, the determination of its amount was possible. This measurement was performed following a methodology successfully used by Attallah et al. [11] on the same material, by properly adjusting the threshold of the SEM micrographs (see for instance Fig. 8), using the software ImageJ. The samples analysed provided a β amount of 27.6% ± 4.5% and 25.8% ± 3.2% for sets A and B, respectively. Therefore, the heat-treated samples appeared similar both in terms of phase composition and lamellar size.

XRD measurements were carried out to further analyse the phases observed. The relative curves, provided in Fig. 9, confirm the hypothesis made about the microstructural transformation that happened during the heat treatment.

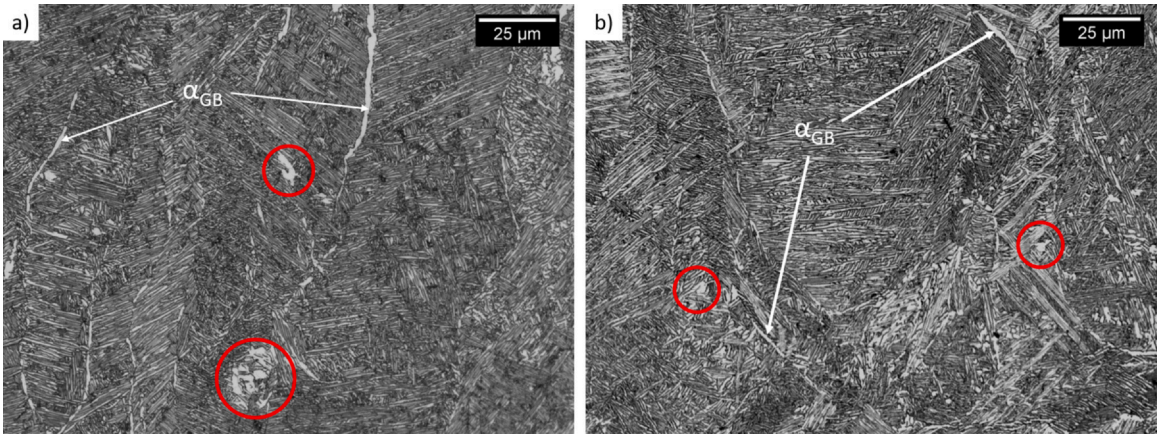

Fig. 6. Optical micrographs of a sample from sets A (a) and B (b) after sub-β annealing; the red circles highlight the small globular α phase.

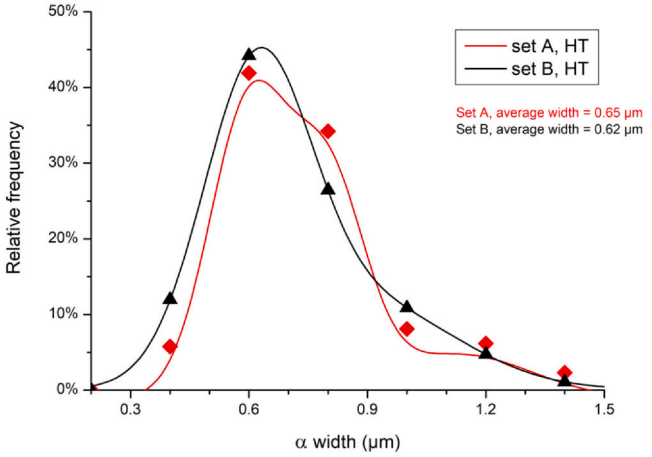

Fig. 7. Relative distribution of lamellar α width for sets A and B.

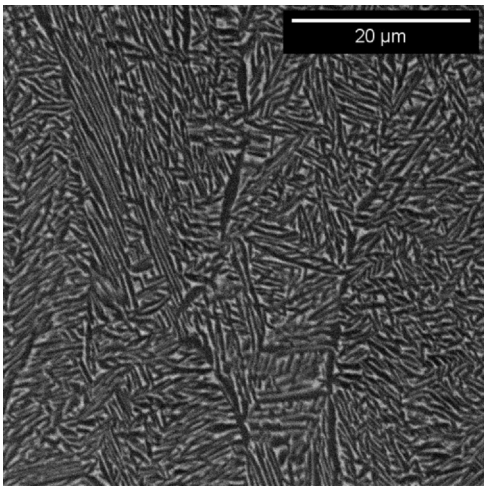

Fig. 8. A representative SEM micrograph of a heat-treated sample.

In the as-built condition, both sets A and B showed only the peaks relative to α" (orthorhombic), confirming a martensitic microstructure. This outcome is consistent with other works available in the literature in which high cooling rates via water quenching were deployed [16,51]. Oppositely, after the heat treatment, in both the groups of specimens α" seems to be completely decomposed into the more stable α and β phases. The (002) peak of the heat-treated

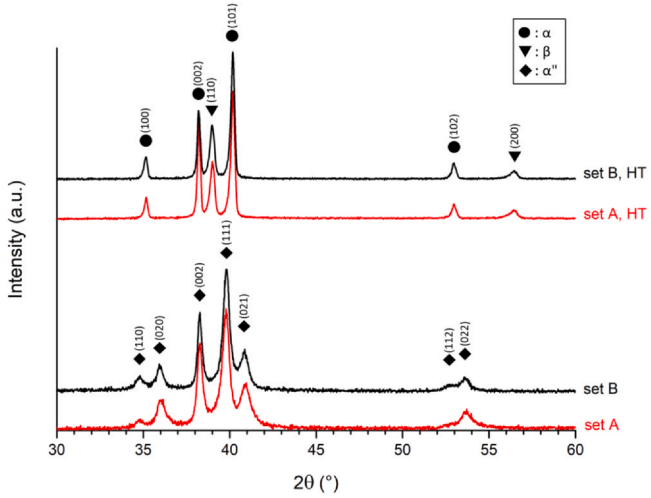

Fig. 9. XRD patterns for sets A and B in the as-built and heat-treated (HT) conditions.

samples, relative to α phase, was relatively higher in set A. Although, this effect can be considered related to texturing.

In order to further investigate the microstructures of these samples, the determination of the cell parameters was carried out using XRD data of the as-built and heat-treated samples. By doing so, possible differences in terms, for example, of cell volume can be assessed. The phase α" was analysed for the as-built specimens, whilst α was chosen to investigate the heat-treated ones. For the latter samples, the β phase was not considered due to the low number of peaks available, which might have resulted in cell values calculations poorly representative from a statistical point of view.

The analytical method to index a crystal is based on the arithmetical manipulation of the Bragg's law, according to the type of lattice involved [52]. For an orthorhombic system, the governing equation is:

$$\sin^2\theta = \frac{\lambda^2}{4}\left(\frac{h^2}{a^2} + \frac{k^2}{b^2} + \frac{l^2}{c^2}\right) \quad (6)$$

Where θ is the diffraction angle relative to the peak considered; h, k and l are its Miller indices; a, b and c are the tetragonal cell parameters and λ is the wavelength of the radiation used in the measurement, 1.5406 Å in this case.

Instead, for a hexagonal system the related equation is:

$$\sin^2\theta = \frac{\lambda^2}{4}\left(\frac{4}{3}\cdot\frac{h^2 + hk + k^2}{a^2} + \frac{l^2}{c^2}\right) \quad (7)$$

Table 4
Cell parameters obtained from the XRD spectra.

Set	Phase	Lattice	Cell parameters (Å)	Cell Volume (Å^3)
A	α"	Orthorhombic	a = 3.029 ± 0.018 b = 4.985 ± 0.007 c = 4.694 ± 0.027	70.787 ± 0.931
B	α"	Orthorhombic	a = 3.005 ± 0.013 b = 4.971 ± 0.013 c = 4.692 ± 0.049	69. 947 ± 1.226
A, HT	α	Hexagonal	a = 2.937 ± 0.045 c = 4.733 ± 0.036	35.345 ± 1.563
B, HT	α	Hexagonal	a = 2.936 ± 0.044 c = 4.733 ± 0.036	35.360 ± 1.550

Where a and c are the hexagonal cell parameters. To minimise the effect of texturing, each parameter was obtained from multiple peaks. This approach is known as the "intensity averaging" method [52]. The results obtained from the cell parameter calculations are reported in Table 4, in which the cell volume for the orthorhombic systems (abc) and the hexagonal systems ($\sqrt{3}\,a^2c/2$) are also listed.

Considering the as-built condition, both sets provided very similar cell parameters, suggesting that the only significant difference among sets A and B lies in the martensite size (as observed in Fig. 5). The calculated cell parameters are also consistent with the data from other works available in the literature in which a martensitic microstructure was obtained through a rapid cooling of the specimens via water quenching [5,17,53]. Another parameter that can be obtained for the as-built samples is the degree of orthorhombicity ($b/a\sqrt{3}$), which equals 1 for hexagonal systems and can be used to investigate the transition from α" (orthorhombic) to α (hexagonal) [17]. The degree of orthorhombicity was 0.950 and 0.955 for sets A and B, respectively. The similarity of these two values highlights that, even if the specimens underwent different cooling paths, their tendency to decompose seemed to be substantially unaffected.

After the heat treatment, sets A and B presented similar cell parameters and volumes, confirming the efficiency of the heat treatment in order to induce uniform microstructures and phase compositions in the LPBF-produced samples.

3.3. Hardness measurement

Hardness measurements were performed on samples from sets A and B in the as-built and heat-treated conditions. The results, reported in Fig. 10, provided an average hardness of 352 ± 15 HV for set A and 328 ± 7 HV for set B as concerning the as-built condition. In these samples the consistent discrepancy in HV is likely caused by the differences in microstructural size (α" width) of the specimens, as visible in Fig. 5. According to the data, using a higher VED during the process lead to lower cooling rates, which resulted in a finer martensitic microstructure that granted higher hardness values.

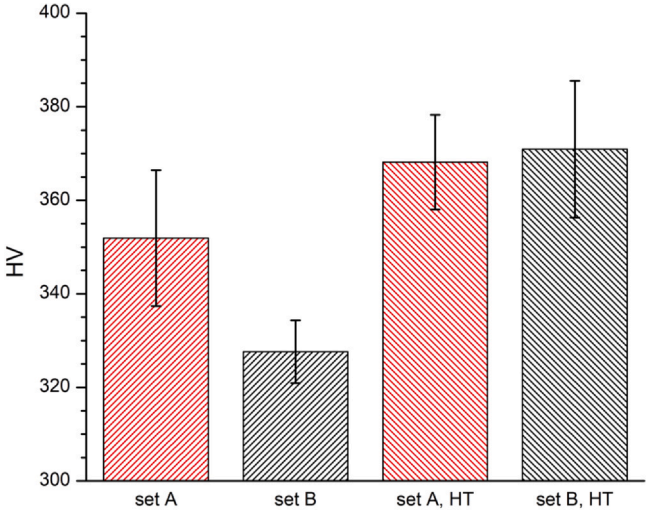

Fig. 10. Average micro-Vickers hardness for sets A and B, in the as-built and heat-treated (HT) conditions.

Considering the heat-treated samples, the hardness was 368 ± 10 HV and 371 ± 14 HV, for sets A and B, respectively. These values were higher than those of the as-built samples, confirming that the absence of α" causes an overall increase in hardness. Moreover, the hardness values of the heat-treated specimens A and B were very close, confirming that the sub-β annealing can effectively erase the differences observed in the as-built conditions induced by the process parameters. Since the main consequence of the annealing was α" decomposition, this effect seems to confirm that the microstructure had a strong influence on HV.

On the basis of the reported results, considering the intrinsic softness of the α" martensite, it is reasonable to state that as-built LPBF-produced Ti6246 is not appropriate for applications in which a high hardness is required. In addition, it was demonstrated that a sub-β annealing, which can also act as a stress-relieving heat treatment [4], erases the differences in microstructure induced by the process parameters adopted. For this reason, opting for the component production with a lower VED, which is usually associated with a higher build-up rate, appears as a cost-effective alternative, as long as porosity is kept under control.

3.4. Tensile test

Tensile tests were conducted on sets A and B, both in the as-built and heat-treated conditions. By looking at the relative curves, visible in Fig. 11a, in the as-built samples a work hardening phenomenon is evident. In general, titanium alloys are prone to be work-hardened, therefore strengthened due to an increase in dislocation density [54]. On the contrary, the heat-treated specimens did not show relevant work hardening, which suggests that this phenomenon is related to the presence of α" martensite.

The Yield Tensile Strength (YTS), Ultimate Tensile Strength (UTS) and ductility (ε) were evaluated from the test outcomes and reported in Fig. 11b and Table 5. Considering the as-built condition, set B was characterized by a greater YTS (582 ± 23 MPa), with respect to set A (483 ± 6 MPa). Instead, in terms of UTS and ε, these samples showed similar values: set A had a UTS and a ε of 1183 ± 7 MPa and 26.9% ± 0.9% respectively. Whilst set B was characterized by a UTS of 1208 ± 11 MPa and a ε of 25.5% ± 0.9%.

The sub-β heat treatment caused a marked increase in the strength of the specimens accounting a YTS of 1052 ± 20 MPa and 1063 ± 10 MPa for sets A and B, respectively. As in the case of the hardness, after the heat treatment the mechanical properties rose to similar values, making the differences generated by using different process parameters negligible. In terms of UTS, the heat treatment caused a slight decrease in both samples, correspondingly 1125 ± 18 MPa and 1146 ± 46 MPa for sets A and B, respectively. Instead, in the heat-treated samples ductility decreased, as expected due to the decomposition of α", which has a softening effect, as mentioned before. Set A was characterized by a ε of 15.5% ± 0.5%, whilst set B had a ε of 16.3% ± 0.5%. In Table 5 the mechanical properties of the conventionally processed material are also presented, for which the wrought + heat-treated conditions were considered [6,55–57]. These presented YTS and UTS values similar to those of the LPBF heat-treated samples. Concerning ductility, the heat-treated LPBF-produced Ti6246 alloy appeared well comparable with the most promising data available in the literature. Hence, the combination of tensile properties achieved suggested that LPBF is a viable alternative to conventional processing for this alloy. This is related to the optimal lamellar microstructure, characterized by fine

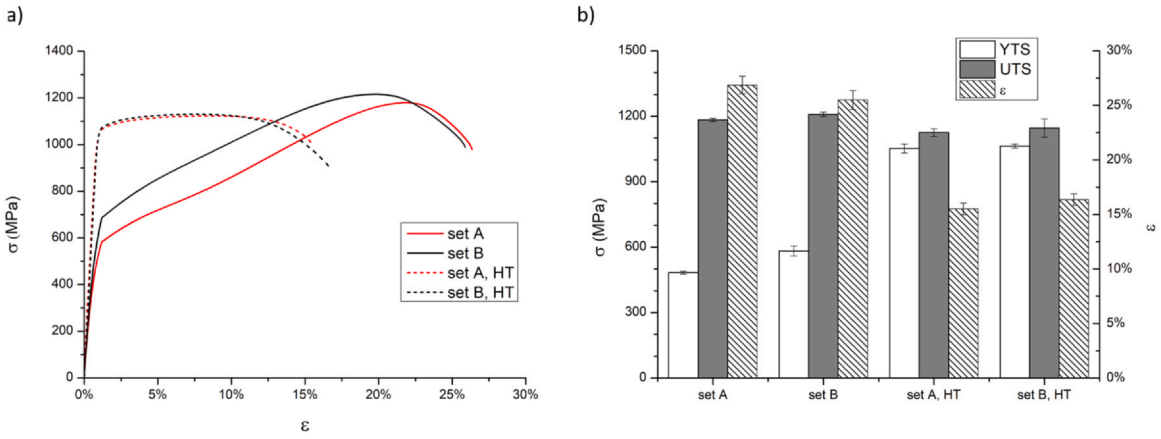

Fig. 11. Tensile curves of the most representative samples (a) and YTS, UTS and ε of all the specimens analysed (b).

Table 5
Mechanical properties obtained from the tensile tests and mechanical properties of the wrought material.

	YTS (MPa)	UTS (MPa)	ε (%)
set A	483 ± 6	1183 ± 7	26.9 ± 0.8
set B	582 ± 23	1209 ± 11	25.5 ± 0.9
set A, HT	1052 ± 20	1125 ± 18	15.5 ± 0.5
set B, HT	1064 ± 10	1146 ± 41	16.4 ± 0.5
conventional [6]	1035	1100	10
conventional [55]	1018	1115	18.4
conventional [56,57]	1062	1131	13

α laths and colonies, in conjunction with the reduced grain size resulting from the LPBF process. These microstructural features are known to promote optimal ductility and strength combinations in duplex titanium alloys [58–60].

As demonstrated, post-processing of the LPBF-produced samples appears as a promising solution in order to achieve good tensile properties.

Indeed, even if the UTS of all the samples are quite close (maximum variation of 6.95%), for structural applications that require high-strength materials, as titanium alloys, YTS is markedly more important, making the heat treatment a mandatory step in order to obtain satisfactory mechanical properties. Moreover, as mentioned before, one of the main advantages of the conventionally-manufactured Ti6246 alloy lies in its higher strength values over the "workhorse" Ti64 alloy. This advantage is the main reason why the former material is appealing in a limited number of industrial fields [7,9]. Thus, a comparison with Ti64 is industrially relevant, when considering LPBF as a manufacturing process instead of a conventional technology. This is mostly due to the unique out-of-equilibrium microstructures achievable using AM techniques, which can result in overall better tensile properties, as in the case of Ti64 [61,62]. Therefore, a comparison between the LPBF-produced Ti6246 tensile properties (YTS, ε), assessed in this work, and those relative to the LPBF-produced Ti64 alloy, available in the literature, was conducted. The aim was to determine whether the superior strength of the former material persisted when moving from a conventional manufacturing process to LPBF. In order to do so, the as-built and heat-treated conditions were considered. Since the two alloys are characterized by different β transus values ($T_{\beta,Ti6246} \simeq 940\,°C$, $T_{\beta,Ti64} \simeq 995\,°C$) [17,63], the heat treatments considered shared the same duration and cooling mean (2 h, slow furnace cooling) but differed in temperature (750 °C for Ti6246 and 800 °C for Ti64). The graphical comparison of the mechanical properties is represented in Fig. 12.

A certain variability between the mechanical properties of the Ti64 alloy was detected. This is an intrinsic consequence of the LPBF technology, as multiple factors can influence the final outcome, such as powder quality and process parameters adopted. The Ti64 as-built specimens were characterised by the highest strength values, ranging from 962 to 1350 MPa. However, for this condition the ductility was markedly lower than the 10% threshold value, defined by ASTM-F2924 [76], which describes the minimum tensile properties to achieve by the Ti64 samples produced using powder bed technologies. This combination of mechanical properties is mostly related to the presence of α' needles and fine grains, induced by the LPBF process. The loss in ductility is related to the reduced dislocation mobility caused by the martensitic needles. The post-processing heat treatment was reported to cause an overall increase of ε, as high as 19% in the Ti64 alloy, but reduced YTS (871–1040 MPa). As described before, the Ti6246 alloy was characterized by an outstanding ductility in the as-printed state, due to the presence of the softening α" phase. After the annealing, the plasticity was reduced, but the YTS approximately doubled, achieving unmatched strength values by the workhorse Ti64 alloy, if reasonable ε values (>10%) are considered. Therefore, it was proved that the Ti6246 alloy is a viable higher-strength alternative to Ti64 even in industrial fields in which LPBF technology can be applied.

4. Conclusions

The aim of this work was to investigate the possibility and feasibility of processing the Ti-6Al-2Sn-4Zr-6Mo alloy using an LPBF system. This alloy can be used in industrial fields in which AM has proved to be a viable manufacturing process. The most important results obtained are:

- Porosity was used as a criterion to determine the most promising process parameters. In this way, multiple combinations of P, v and h.d. were found to provide satisfactory relative density values. In particular, porosity minimisation is achieved more efficiently at higher VED values.
- VED also influences the pore shape. The data suggests that higher VED values lead to the production of samples characterised by pores overall closer to sphericity.
- Microstructural features typical of LPBF-produced titanium alloys (e.g. Ti-6Al-4V) were also obtained for Ti-6Al-2Sn-4Zr-6Mo. In particular, prior-β grains, characterised by a columnar morphology and a completely martensitic microstructure were detected. The main difference between this alloy and most of the other α + β alloys lies in the type of martensite, which is orthorhombic (α") instead of hexagonal.
- VED, hence the process parameters, has a direct impact on the final microstructure. In particular, higher VED values provide finer α" needles in the as-built condition.

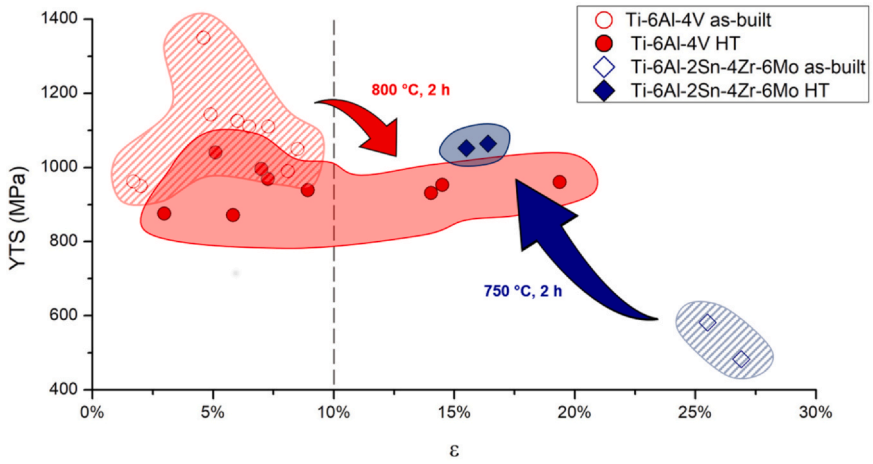

Fig. 12. Graphical comparison of the tensile properties of the LPBF-produced Ti6246 and Ti64 alloys in the as-built [64–72] and heat-treated (HT) [72–75] conditions. The dashed line represents the ductility minimum threshold described by ASTM-F2924 [76].

- A heat treatment at 750 °C for 2 h, followed by slow furnace cooling, provides complete martensite decomposition, turning the microstructure into lamellar α + β. The size of the lamellae of the α phase is independent from the initial α" size.
- The microstructure obtained through the heat treatment is characterised mainly by lamellar α + β. Apart from α laths, this phase is also present as α_{GB} and occasionally in small globular features.
- In the as-built state, hardness is dependent on the size distribution of the martensite, hence the process parameters. This effect is erased by the heat treatment, which balances the hardness of the samples built using different process parameters and leads to an increase in hardness by getting rid of the soft α" phase.
- The as-built samples show markedly low yield strength values but extensive ductility. Instead, the heat-treated specimens are characterised by a markedly higher YTS, although ductility is reduced.
- The heat-treated LPBF-produced specimens show comparable strength values with the wrought material. However, the ductility was markedly higher in the samples produced by LPBF. Therefore, this technology appears very promising in order to obtain components characterised by an optimal combination of strength and ductility.
- The LPBF-produced Ti6246 alloy, after a post-processing heat treatment, provides higher tensile strength values than Ti64 in similar conditions. Since this criterion is the main reason why the former material is used in some industrial applications, the Ti6246 alloy remains relevant even if an LPBF system is adopted instead of using a conventional manufacturing technology.

Funding

This research was funded by Horizon 2020 research and innovation program with grant number 820774.

CRediT authorship contribution statement

Alessandro Carrozza: Conceptualization, Methodology, Validation, Formal analysis, Investigation, Writing - original draft, Visualization. **Alberta Aversa**: Conceptualization, Methodology, Writing - review & editing. **Paolo Fino**: Resources, Supervision. **Mariangela Lombardi**: Conceptualization, Resources, Writing - review & editing, Project administration, Funding acquisition.

Declaration of Competing Interest

The authors declare that they have no known competing financial interests or personal relationships that could have appeared to influence the work reported in this paper.

Acknowledgments

The authors would like to acknowledge the European research project MANUELA Additive Manufacturing using Metal Pilot Line (Project ID 820774) which received funding from the European Union's Horizon 2020 research and innovation program.

References

[1] C. Leyens, M. Peters, Titanium and titanium alloys: fundamentals and applications, 2003.
[2] R. Pederson, F. Niklasson, F. Skystedt, R. Warren, Microstructure and mechanical properties of friction- and electron-beam welded Ti-6Al-4V and Ti-6Al-2Sn-4Zr-6Mo, Mater. Sci. Eng. A 552 (2012) 555–565, https://doi.org/10.1016/j.msea.2012.05.087
[3] R.P. Kolli, A. Devaraj, A review of metastable beta titanium alloys, Metals 8 (2018) 1–41, https://doi.org/10.3390/met8070506
[4] F.H. Froes, Titanium: Physical Metallurgy Processing and Application, 2015.
[5] A.K. Dutt, B. Gwalani, V. Tungala, M. Carl, R.S. Mishra, S.A. Tamirisakandala, M.L. Young, K.C. Cho, R.E. Brennan, A novel nano-particle strengthened titanium alloy with exceptional specific strength, Sci. Rep. 9 (2019) 1–9, https://doi.org/10.1038/s41598-019-48139-8
[6] R. Boyer, G. Welsch, E.W. Collings, Materials properties handbook: titanium alloys, 1994.
[7] G. Lütjering, J.C. Williams, Titanium, Springer, 2007, https://doi.org/10.10007/978-3-540-71398-2
[8] S. Birosca, J.Y. Buffiere, F.A. Garcia-Pastor, M. Karadge, L. Babout, M. Preuss, Three-dimensional characterization of fatigue cracks in Ti-6246 using X-ray tomography and electron backscatter diffraction, Acta Mater. 57 (2009) 5834–5847, https://doi.org/10.1016/j.actamat.2009.08.009
[9] M.J. Donachie, A guide to engineering selection of titanium alloys for design, Mechanical Engineer's Handbook, Wiley Online Library, 2014, pp. 1–37.
[10] R. Pederson, The microstructures of Ti-6Al-4V and Ti-6Al-2Sn-4Zr-6Mo and their relationship to processing and properties, 2004. doi:ISSN 1402–1544 / ISRN LTU-DT–04/19–SE / NR 2004:19.
[11] M.M. Attallah, S. Zabeen, R.J. Cernik, M. Preuss, Comparative determination of the α/β phase fraction in α+β-titanium alloys using X-ray diffraction and electron microscopy, Mater. Charact. 60 (2009) 1248–1256, https://doi.org/10.1016/j.matchar.2009.05.006
[12] J.C. Williams, A.F. Belov, Titanium and Titanium Alloys: Scientific and Technological Aspects., 1982.
[13] J. Yang, H. Yu, J. Yin, M. Gao, Z. Wang, X. Zeng, Formation and control of martensite in Ti-6Al-4V alloy produced by selective laser melting, Mater. Des. 108 (2016) 308–318, https://doi.org/10.1016/j.matdes.2016.06.117
[14] E. Salsi, M. Chiumenti, M. Cervera, Modeling of microstructure evolution of Ti6Al4V for additive manufacturing, Metals 8 (2018) 633, https://doi.org/10.3390/met8080633
[15] S. Bein, J. Bechet, Phase transformation kinetics and mechanisms in titanium alloys Ti-6.2.4.6,ß-CEZ and Ti-10.2.3, J. Phys. IV Fr. 06 (1996) C1–99-C1-108.

[16] Y. Ito, Y. Moriguchi, N. Takashi, The Effect of Microstructures on Mechanical Properties of the β rich α-β Titanium alloy of Ti-6Al-2Sn-4Zr-6Mo, (1986) 1–8.
[17] M. Young, E. Levine, H. Margolin, Aging behavior of orthorhombic martensite in Ti-6-2-4-6, Met. Trans. 5 (1974) 1891–1898, https://doi.org/10.1007/BF02644157
[18] Y. Guo, T. Jung, Y.L. Chiu, H. Li, S. Bray, P. Bowen, Microstructure and microhardness of Ti6246 linear friction weld, Mater. Sci. Eng. A 562 (2013) 17–24, https://doi.org/10.1016/j.msea.2012.10.089
[19] W.E. Frazier, Metal additive manufacturing: a review, J. Mater. Eng. Perform. 23 (2014) 1917–1928, https://doi.org/10.1007/s11665-014-0958-z
[20] F.G. Arcella, F.H. Froes, Producing titanium aerospace components from powder using laser forming, JOM 52 (2000) 28–30, https://doi.org/10.1007/s11837-000-0028-x
[21] Y. Zhao, Z. Ma, L. Yu, J. Dong, Y. Liu, The simultaneous improvements of strength and ductility in additive manufactured Ni-based superalloy via controlling cellular subgrain microstructure, J. Mater. Sci. Technol. 68 (2021) 184–190, https://doi.org/10.1016/j.jmst.2020.07.011
[22] G. Marchese, S. Parizia, M. Rashidi, A. Saboori, D. Manfredi, D. Ugues, M. Lombardi, E. Hryha, S. Biamino, The role of texturing and microstructure evolution on the tensile behavior of heat-treated Inconel 625 produced via laser powder bed fusion, Mater. Sci. Eng. A 769 (2020) 138500.
[23] K. Schmidtke, F. Palm, A. Hawkins, C. Emmelmann, Process and mechanical properties: applicability of a scandium modified Al-alloy for laser additive manufacturing, Phys. Procedia 12 (2011) 369–374.
[24] A. Aversa, G. Marchese, D. Manfredi, M. Lorusso, F. Calignano, S. Biamino, M. Lombardi, P. Fino, M. Pavese, Laser powder bed fusion of a high strength Al-Si-Zn-Mg-Cu alloy, Metals 8 (2018) 300.
[25] K.M. Bertsch, G. Meric de Bellefon, B. Kuehl, D.J. Thoma, Origin of dislocation structures in an additively manufactured austenitic stainless steel 316L, Acta Mater. 199 (2020) 19–33, https://doi.org/10.1016/j.actamat.2020.07.063
[26] Y. He, M. Zhong, J. Beuth, B. Webler, A study of microstructure and cracking behavior of H13 tool steel produced by laser powder bed fusion using single-tracks, multi-track pads, and 3D cubes, J. Mater. Process. Technol. 286 (2020) 116802.
[27] C.M. Cepeda-Jiménez, F. Potenza, E. Magalini, V. Luchin, A. Molinari, M.T. Pérez-Prado, Effect of energy density on the microstructure and texture evolution of Ti-6Al-4V manufactured by laser powder bed fusion, Mater. Charact. 163 (2020) 110238.
[28] C. de Formanoir, U. Paggi, T. Colebrants, L. Thijs, G. Li, K. Vanmeensel, B. Van Hooreweder, Increasing the productivity of laser powder bed fusion: Influence of the hull-bulk strategy on part quality, microstructure and mechanical performance of ti-6al-4v, Addit. Manuf. 33 (2020) 101129, https://doi.org/10.1016/j.addma.2020.101129
[29] S.E. Brika, M. Letenneur, C.A. Dion, V. Brailovski, Influence of particle morphology and size distribution on the powder flowability and laser powder bed fusion manufacturability of Ti-6Al-4V alloy, Addit. Manuf. 31 (2020) 100929.
[30] Y. Xiao, N. Dai, Y. Chen, J. Zhang, S.-W. Choi, On the microstructure and corrosion behaviors of selective laser melted CP-Ti and Ti-6Al-4V alloy in Hank's artificial body fluid, Mater. Res. Express 6 (2019) 126521.
[31] T. Marcu, M. Todea, I. Gligor, P. Berce, C. Popa, Effect of surface conditioning on the flowability of Ti6Al7Nb powder for selective laser melting applications, Appl. Surf. Sci. 258 (2012) 3276–3282.
[32] L.C. Zhang, D. Klemm, J. Eckert, Y.L. Hao, T.B. Sercombe, Manufacture by selective laser melting and mechanical behavior of a biomedical Ti–24Nb–4Zr–8Sn alloy, Scr. Mater. 65 (2011) 21–24.
[33] M. Speirs, J. Van Humbeeck, J. Schrooten, J. Luyten, J.-P. Kruth, The effect of pore geometry on the mechanical properties of selective laser melted Ti-13Nb-13Zr scaffolds, Procedia CIRP 5 (2013) 79–82.
[34] A.W. Gebisa, H.G. Lemu, Additive manufacturing for the manufacture of gas turbine engine components: Literature review and future perspectives, Proc. ASME Turbo Expo. 6 (2018) 1–10. doi:10.1115/GT2018–76686.
[35] A. Carrozza, A. Saboori, S. Biamino, M. Lombardi, A. Aversa, G. Marchese, M. Cooper, L. Howlett, Advanced Powder Characterization for Laser Powder-Bed Fusion of AlSi10Mg, in: Eur. 2018, European Powder Metallurgy Association (EPMA), Bilbao, 2018.
[36] S. Palanivel, A.K. Dutt, E.J. Faierson, R.S. Mishra, Spatially dependent properties in a laser additive manufactured Ti-6Al-4V component, Mater. Sci. Eng. A 654 (2016) 39–52, https://doi.org/10.1016/j.msea.2015.12.021
[37] Standard test methods for tension testing of metallic materials, Annu. B. ASTM Stand, ASTM, 2001.
[38] A.E. Wilson-Heid, Z. Wang, B. McCornac, A.M. Beese, Quantitative relationship between anisotropic strain to failure and grain morphology in additively manufactured Ti-6Al-4V, Mater. Sci. Eng. A 706 (2017) 287–294, https://doi.org/10.1016/j.msea.2017.09.017
[39] B. Shen, H. Li, S. Liu, J. Zou, S. Shen, Y. Wang, T. Zhang, D. Zhang, Y. Chen, H. Qi, Influence of laser post-processing on pore evolution of Ti–6Al–4V alloy by laser powder bed fusion, J. Alloy. Compd. 818 (2020) 152845, https://doi.org/10.1016/j.jallcom.2019.152845
[40] ISO 9276–6:2008 Representation of results of particle size analysis — Part 6: Descriptive and quantitative representation of particle shape and morphology, (n.d.).
[41] G. Kasperovich, J. Haubrich, J. Gussone, G. Requena, Correlation between porosity and processing parameters in TiAl6V4 produced by selective laser melting, Mater. Des. 105 (2016) 160–170.
[42] F. Trevisan, F. Calignano, A. Aversa, G. Marchese, M. Lombardi, S. Biamino, D. Ugues, D. Manfredi, Additive manufacturing of titanium alloys in the biomedical field: processes, properties and applications, J. Appl. Biomater. Funct. Mater. 16 (2018) 57–67, https://doi.org/10.5301/jabfm.5000371
[43] S. Liu, Y.C. Shin, Additive manufacturing of Ti6Al4V alloy: a review, Mater. Des. 164 (2018) 8–12, https://doi.org/10.1016/j.matdes.2018.107552
[44] P.A. Hooper, Melt pool temperature and cooling rates in laser powder bed fusion, Addit. Manuf. 22 (2018) 548–559, https://doi.org/10.1016/j.addma.2018.05.032
[45] M.V. Pantawane, Y.H. Ho, S.S. Joshi, N.B. Dahotre, Computational assessment of thermokinetics and associated microstructural evolution in laser powder bed fusion manufacturing of Ti6Al4V alloy, Sci. Rep. 10 (2020) 1–14, https://doi.org/10.1038/s41598-020-63281-4
[46] A. Carrozza, A. Aversa, F. Mazzucato, M. Lombardi, S. Biamino, A. Valente, P. Fino, An innovative approach on directed energy deposition optimization: a study of the process environment's influence on the quality of Ti-6Al-4V samples, Appl. Sci. 10 (2020) 4212.
[47] K. Wei, Z. Wang, F. Li, H. Zhang, X. Zeng, Densification behavior, microstructure evolution, and mechanical performances of selective laser melted Ti-5Al-2.5Sn α titanium alloy: effect of laser energy input, J. Alloy. Compd. 774 (2019) 1024–1035, https://doi.org/10.1016/j.jallcom.2018.09.153
[48] V. Thampy, A.Y. Fong, N.P. Calta, J. Wang, A.A. Martin, P.J. Depond, A.M. Kiss, G. Guss, Q. Xing, R.T. Ott, A. van Buuren, M.F. Toney, J.N. Weker, M.J. Kramer, M.J. Matthews, C.J. Tassone, K.H. Stone, Subsurface cooling rates and microstructural response during laser based metal additive manufacturing, Sci. Rep. 10 (2020) 1–9, https://doi.org/10.1038/s41598-020-58598-z
[49] Y. Li, L. Song, P. Xie, M. Cheng, H. Xiao, Enhancing hardness and wear performance of laser additive manufactured Ti6Al4V alloy through achieving ultrafine microstructure, Materials 13 (2020) 15–18, https://doi.org/10.3390/ma13051210
[50] C. Sauer, G. Lütjering, Influence of α layers at β grain boundaries on mechanical properties of Ti-alloys, Mater. Sci. Eng. A 319–321 (2001) 393–397, https://doi.org/10.1016/S0921-5093(01)01018-8
[51] P. Stella, I. Giovanetti, G. Masi, M. Leoni, A. Molinari, Microstructure and microhardness of heat-treated Ti-6Al-2Sn-4Zr-6Mo alloy, J. Alloy. Compd. 567 (2013) 134–140, https://doi.org/10.1016/j.jallcom.2013.03.046
[52] B.D. Cullity, S.R. Stock, Elements of X-Ray Diffraction, Addison-Wesley Publishing, 1956.
[53] X. Ji, I. Gutierrez-Urrutia, S. Emura, T. Liu, T. Hara, X. Min, D. Ping, K. Tsuchiya, Twinning behavior of orthorhombic-α" martensite in a Ti-7.5Mo alloy, Sci. Technol. Adv. Mater. 20 (2019) 401–411, https://doi.org/10.1080/14686996.2019.1600201
[54] W. Sha, S. Malinov, Titanium Alloys: Modelling of Microstructure, Properties and Applications, Elsevier, 2009.
[55] S. Hémery, P. Villechaise, Comparison of slip system activation in Ti-6Al-2Sn-4Zr-2Mo and Ti-6Al-2Sn-4Zr-6Mo under tensile, fatigue and dwell-fatigue loadings, Mater. Sci. Eng. A 697 (2017) 177–183.
[56] R.B. Sparks, J.R. Long, Improved Manufacturing Methods for Producing High Integrity More Reliable Forgings, Technical Report AFML-TR-73–301, Air Force Materials Laboratory, Wright …, 1974.
[57] A.K. Vasudevan, R.D. Doherty, Aluminum Alloys-Contemporary Research and Applications, Elsevier, 2012.
[58] R. Filip, K. Kubiak, W. Ziaja, J. Sieniawski, The effect of microstructure on the mechanical properties of two-phase titanium alloys, J. Mater. Process. Technol. 133 (2003) 84–89, https://doi.org/10.1016/S0924-0136(02)00248-0
[59] G. Lütjering, Influence of processing on microstructure and mechanical properties of (α+ β) titanium alloys, Mater. Sci. Eng. A 243 (1998) 32–45.
[60] S. Raghavan, M.L.S. Nai, P. Wang, W.J. Sin, T. Li, J. Wei, Heat treatment of electron beam melted (EBM) Ti-6Al-4V: microstructure to mechanical property correlations, Rapid Prototyp. J. 24 (2018) 774–783, https://doi.org/10.1108/RPJ-05-2016-0070
[61] L.C. Zhang, Y. Liu, S. Li, Y. Hao, Additive manufacturing of titanium alloys by electron beam melting: a review, Adv. Eng. Mater. 20 (2018) 1–16, https://doi.org/10.1002/adem.201700842
[62] L.C. Zhang, H. Attar, M. Calin, J. Eckert, Review on manufacture by selective laser melting and properties of titanium based materials for biomedical applications, Mater. Technol. 31 (2016) 66–76, https://doi.org/10.1179/1753555715Y.0000000076
[63] S.L. Semiatin, V. Seetharaman, I. Weiss, Hot working of titanium alloys - an overview, Adv. Sci. Technol. Titan. Alloy Process (1996) 3–73.
[64] B. Vrancken, L. Thijs, J.P. Kruth, J. Van Humbeeck, Heat treatment of Ti6Al4V produced by selective laser melting: microstructure and mechanical properties, J. Alloy. Compd. 541 (2012) 177–185, https://doi.org/10.1016/j.jallcom.2012.07.022
[65] C. Qiu, N.J.E.E. Adkins, M.M. Attallah, Microstructure and tensile properties of selectively laser-melted and of HIPed laser-melted Ti–6Al–4V, Mater. Sci. Eng. A 578 (2013) 230–239, https://doi.org/10.1016/j.msea.2013.04.099
[66] T. Vilaro, C. Colin, J.D. Bartout, As-fabricated and heat-treated microstructures of the Ti-6Al-4V alloy processed by selective laser melting, Metall. Mater. Trans. A Phys. Metall. Mater. Sci. 42 (2011) 3190–3199, https://doi.org/10.1007/s11661-011-0731-y
[67] H.K. Rafi, N.V. Karthik, H. Gong, T.L. Starr, B.E. Stucker, Microstructures and mechanical properties of Ti6Al4V parts fabricated by selective laser melting and electron beam melting, J. Mater. Eng. Perform. 22 (2013) 3872–3883, https://doi.org/10.1007/s11665-013-0658-0
[68] L. Facchini, E. Magalini, P. Robotti, A. Molinari, S. Höges, K. Wissenbach, Ductility of a Ti-6Al-4V alloy produced by selective laser melting of prealloyed powders, Rapid Prototyp. J. 16 (2010) 450–459, https://doi.org/10.1108/13552541011083371
[69] L.E. Murr, S.A. Quinones, S.M. Gaytan, M.I. Lopez, A. Rodela, E.Y. Martinez, D.H. Hernandez, E. Martinez, F. Medina, R.B. Wicker, Microstructure and mechanical behavior of Ti-6Al-4V produced by rapid-layer manufacturing, for

biomedical applications, J. Mech. Behav. Biomed. Mater. 2 (2009) 20–32, https://doi.org/10.1016/j.jmbbm.2008.05.004
[70] D.A. Hollander, M. Von Walter, T. Wirtz, R. Sellei, B. Schmidt-Rohlfing, O. Paar, H.J. Erli, Structural, mechanical and in vitro characterization of individually structured Ti-6Al-4V produced by direct laser forming, Biomaterials 27 (2006) 955–963, https://doi.org/10.1016/j.biomaterials.2005.07.041
[71] B. Vandenbroucke, J.P. Kruth, Selective laser melting of biocompatible metals for rapid manufacturing of medical parts, Rapid Prototyp. J. 13 (2007) 196–203, https://doi.org/10.1108/13552540710776142
[72] S. Cao, Z. Chen, C.V.S. Lim, K. Yang, Q. Jia, T. Jarvis, D. Tomus, X. Wu, Defect, microstructure, and mechanical property of Ti-6Al-4V alloy fabricated by high-power selective laser melting, JOM 69 (2017) 2684–2692, https://doi.org/10.1007/s11837-017-2581-6
[73] S. Cao, R. Chu, X. Zhou, K. Yang, Q. Jia, C.V.S. Lim, A. Huang, X. Wu, Role of martensite decomposition in tensile properties of selective laser melted Ti-6Al-4V, J. Alloy. Compd. 744 (2018) 357–363.
[74] X. Yan, S. Yin, C. Chen, C. Huang, R. Bolot, R. Lupoi, M. Kuang, W. Ma, C. Coddet, H. Liao, Effect of heat treatment on the phase transformation and mechanical properties of Ti6Al4V fabricated by selective laser melting, J. Alloy. Compd. 764 (2018) 1056–1071.
[75] M. Thöne, S. Leuders, A. Riemer, T. Tröster, H.A. Richard, Influence of heat-treatment on Selective Laser Melting products–eg Ti6Al4V, in: Solid Free. Fabr. Symp. SFF, Austin Texas, 2012.
[76] ASTM F2924–12, Standard Specification for Additive Manufacturing Titanium-6 Aluminum-4 Vanadium with Powder Bed Fusion, ASTM Int. i (2012) 1–9. doi:10.1520/F2924–14.2.